ADVANCED MATERIALS INTERFACES
www.advmatinterfaces.de

Single Iron Atom Anchored on ZIF-8 Derived Carbon Framework to Directionally Regulate Lithium Deposition with Minimum Nucleation Overpotential

Zhixing Guan, Zaka Ullah, Surong Zheng, Ruizai Yang, Penghao Zhu, Qing Cheng, Penghao Song, Qi Li, and Liwei Liu*

Lithium (Li) metal has earned valuable status among the most auspicious anodes for the assembly of next-generation rechargeable batteries. However, the dendritic growth and infinite change in volume of metallic Li anode strongly hinder its use for practical applications. Here, the preparation of atomically dispersed iron doped ZIF-8 through pyrolysis (Fe@NC) to lower the Li nucleation overpotential and control the Li deposition on specific positions is reported. Thermodynamic and kinetic simulations show that the doped single Fe atoms can improve the atomic structure, increase the adsorption energy and enhance the diffusion capacity of Li. Moreover, the specific framework structure of Fe@NC can induce Li metal to nucleate in interior space of the material which can hinder the Li growth along one direction and restrain its volume expansion. As-fabricated electrode displays nearly no nucleation overpotential at current density of 2 mA cm^{-2} and offers higher average Coulombic efficiency up to 99.0% for 100 cycles at current density 2 mA cm^{-2}, and higher areal capacity up to 5 mAh cm^{-2}. Also, the fabricated Fe@NC/LiFePO$_4$ based full cells exhibit a longer lifespan of 100 cycles at 0.5 C. The results provide new insights for future rechargeable Li metal batteries.

1. Introduction

Exponentially increasing demands of energy are not letting the researchers to meet the requirements for future energy storage devices, especially high-energy-density rechargeable batteries.[1–4] Li anodes owing to their remarkably higher theoretical specific capacity (3860 mAh g^{-1}) and significantly lower redox potential (−3.04 V vs typical hydrogen electrode),[5,6] are considered as the most promising candidates in this regard. These are capable of being paired up with most of the desired cathode materials including oxygen,[7–9] sulfur,[10–12], and carbon dioxide.[13,14] However, for practical batteries, Li metal anodes face extensive challenges particularly heterogeneous nucleation and unavoidable dendritic growth during electrochemical plating/stripping process.[15–18] The uncontrollable growth of dendrites causes irreversible capacity loss, low Coulombic efficiency, serious volumetric change, and repeated consumption of electrolytes.[19] More alarmingly, the dendrites may penetrate into the separator which may further lead to internal short-circuit and hence fatal failure of the battery devices.

Considerable efforts have been made to address the challenging issues of Li dendrites, including introduction of additives into electrolytes to build stable solid-state electrolyte interface (SEI) films,[20,21] construction of stabilized artificial SEI to hinder dendrite penetration,[22–24] and application of highly porous conductive matrix to make uniform Li deposition.[25–27] However, directional control of lithium deposition remained elusive till now. The systematic study of Li nucleation behavior has become essential for spontaneously guiding Li deposition to control the morphology as well as position.

Recently, single-atom catalysts combined with non-noble metal monodispersed single atoms were claimed to improve the lithiophilicity of matrix by increasing the adsorption energy between the Li atoms and matrix, which benefits the nucleation rate and hence growth of Li metal with a decreased overpotential. The doped metal single atoms can be combined with nitrogen (N) to form metal−N$_x$−C sites which can affect the electronic cloud around the doping sites. However, the key approaches of past investigations are mainly based on thermodynamic analyses. The kinetic factors like the diffusion capacity of Li on matrix have often been overlooked.[28–31]

It is well-accepted that the resultant morphology of deposited Li is associated with its initial nucleation behavior. The matrix of Li deposition has a profound effect on nuclei size and nucleation behavior of Li. However, for most of the single-atom catalysts, the substrates are carbon-based materials with lamellar stacking structure (e.g., graphene) in which lithium ions have enough

Z. Guan, S. Zheng, R. Yang, P. Zhu, Q. Cheng, P. Song, Q. Li, L. Liu
Key Laboratory of Nanodevices and Applications and Collaborative Innovation Center of Suzhou Nano Science and Technology
Suzhou Institute of Nano-Tech and Nano-Bionics
Chinese Academy of Sciences (CAS)
Suzhou 215123, China
E-mail: qli2013@sinano.ac.cn

Z. Ullah
Department of Physics
Division of Science and Technology
University of Education
Lahore 54770, Pakistan

The ORCID identification number(s) for the author(s) of this article can be found under https://doi.org/10.1002/admi.202201278.

DOI: 10.1002/admi.202201278

chances to diffuse through the basal plane via defects. In such cases, the defect sites form steric hindrance to hinder the diffusion parallel to the plane. This may result in surface structure damage during long-term cycling which will limit the application of battery. In this scenario, hunting of lithiophilic 3D carbonaceous matrix has become of great need and significance.[32–35]

Zeolitic imidazolate frameworks (ZIFs) are 3D crystalline metal organic frameworks (MOFs) with nanoporous morphology, uniformly structured cavities, extremely higher surface area, good mechanical and thermal stability, and well-distributed N-containing functional groups to provide doping sites.[36,37] Herein, we employed ZIF-8 as a carrier to let single iron (Fe) atoms anchored on it, and treated the obtained material with the method of thermal pyrolysis in order to assemble Fe@NC. The single Fe atom can form a coordination bond with surrounding N to enhance the adsorption energy, decrease the nucleation barrier, improve the atomic structural stability, and increase the diffusion capacity of Li. The homogeneously distributed single Fe atoms can induce Li metal to nucleate into the interior space of Fe@NC where remarkable framework structure contributes to hinder the Li growth over one direction and restrain the Li metal volume expansion. Besides, superior 3D porous structure of Fe@NC endows Li to be integrated into electrode without affecting subsequent cycling, thus decreasing the amount of Li deposition on electrode surface and suppressing the dendrites, as shown in **Figure 1**. As a consequence, the Fe@NC electrode exhibits nearly no nucleation overpotential at an applied current density of 2 mA cm^{-2}, and delivers a notable average Coulombic efficiency of 99.0% for 100 provided cycles at a current density 2 mA cm^{-2}. The areal capacity of the electrode remained as high as 5 mAh cm^{-2}. Besides, full cells based on Fe@NC/$LiFePO_4$ exhibited a longer lifetime of 100 cycles provided at 0.5 C.

2. Results and Discussion

2.1. Regional Nucleation Mechanism of Single Fe Atom Doped NC

To investigate the intrinsic mechanisms of uniform Li deposition persuaded by Fe@NC, density functional theory (DFT) investigations were employed. At the start, Li adsorption energy of Fe@NC and NC was calculated and compared with cohesive energy of Li atom in Li metal (–1.83 eV, more details in Experimental Section). The Li adsorption energy which is greater than Li cohesive energy, makes it more probable for Li atoms to be nucleated at host material surface instead of bulk Li. The computational simulation results given in **Figure 2**a–d shows the lithium adsorption energy of NC as –2.07 eV (Table S1, Supporting Information) which is larger than Li cohesive energy (with a difference of –0.24 eV). This implies that the Li cluster can easily be detached from NC collector which will result in the formation of Li dendrites and isolation of Li particles ("dead Li"). Moreover, Fe@NC displays a comparatively larger Li adsorption energy (2.28 eV) which indicates the favorable lithiophilicity of this matrix, and suggests that Li atoms will prefer to be deposited around the isolated and randomly distributed Fe—N_x—C sites. Such a situation will discourage the formation of dendrites.

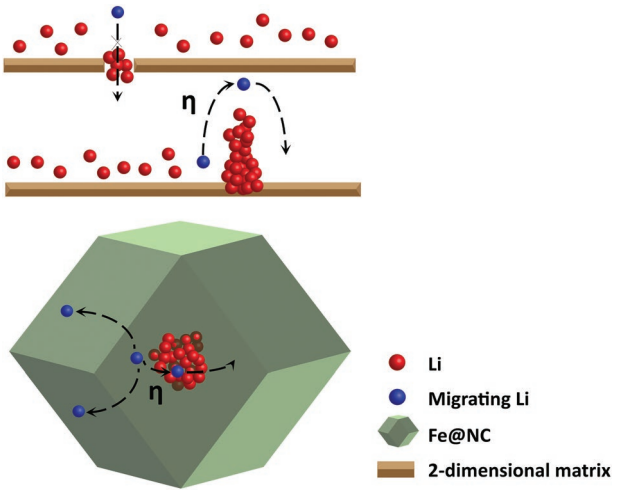

Figure 1. Schematic diagram of Li plating process on 2D matrix and Fe@NC.

To further study how the Fe@NC matrix can enhance the adsorption ability of Li, the charge density difference between NC and Fe@NC was investigated, as shown in Figure 2e,f. The adsorption of Li on Fe@NC or NC is the process of charge transfer from Li atom to the intermediate region between lithium and substrate. The adsorption process leads to develop different electronic states in Li as per the electronegativity difference of Fe (1.83), N (3.04), C (2.54), and Li (0.98). As the Li has smallest electronegativity among these elements, the region around the Fe—N_x—C sites exhibits a strong adsorption impact for Li atom, leading to the enhancement in the adsorption ability of Li. Nevertheless, the atomic structural stability of N and C might be affected by strong N—C bond in NC material. Consequently, the variations in the bond length of N and C in Fe@NC and NC were also calculated. After the adsorption of Li atoms, the N—C bond in the NC deforms severely (Figure 2c,d; Figure S1, Supporting Information). The bond length of N and C was increased by 0.008 Å in Fe@NC (Table S2, Supporting Information) which is much smaller as compared to that in NC (0.055 Å). This evidences that single ion doping can enhance the structural stability of Fe@NC.

In addition to the thermodynamic properties, the kinetic properties of the electrode materials also have a critical effect on the initial nucleation rate of lithium. Consequently, the diffusion energy barrier of Li was computed to investigate its diffusion ability both in Fe@NC and NC materials. Figure 2g,h shows that the diffusion energy barrier of Li on Fe@NC is 0.486 eV which is much lower than that of NC (3.621 eV). This suggests that Li atoms can easily diffuse through the Fe@NC matrix. This phenomenon will oppose the aggregation of Li atoms in one position and may have a positive effect on fast-charging field. All these results strongly suggest that the single Fe atom doped Fe@NC as anode material may offer great potential for Li metal battery.

2.2. Compositional and Structural Characterization

The $Fe(acac)_3$, $Zn(NO_3)_2 \cdot 6H_2O$, and 2-methylimidazole were dissolved in methanol for the synthesis of Fe@NC (see more details in Experimental Section). **Figure 3**a and Figure S2 (Supporting Information) show that the as-prepared

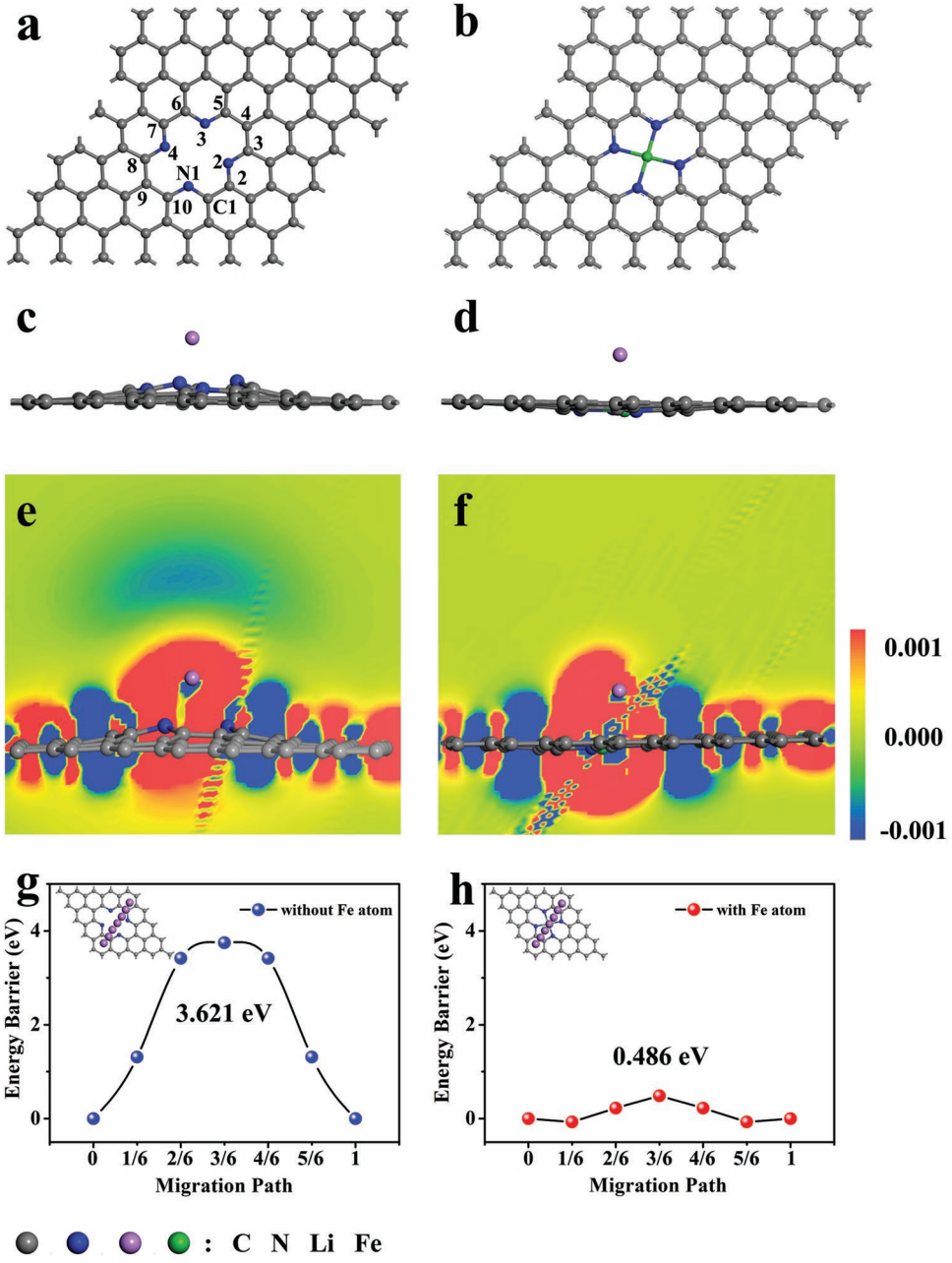

Figure 2. Top views of a) NC, and b) Fe@NC. Side views of c) NC, and d) Fe@NC after Li adsorption. Cross-sectional observation of charge density distribution of Li atoms adsorbed on e) NC, and f) Fe@NC. Red and blue colors respectively denote the charge accumulation and loss regions. Isosurface value is set as 0.001 e Å^{-3}. Change in energy upon diffusion of adsorbed lithium atoms along the matrix of g) NC, and h) Fe@NC. Inset images are the diffusion pathway of Li atom on the matrix.

Fe@NC exhibits the structure of hexagonal shape which is similar to that of NC (Figures S3 and S4, Supporting Information). High-resolution transmission electron microscopy (HRTEM) view given in Figure 3b evidences that there are no obvious iron-based metal nanoparticles. However, there are massive micropores on Fe@NC surface which evidence the doping of Fe in NC at atomic level, and porous structure of Fe@NC. Moreover, atomic-resolution high-angle annular dark-field scanning transmission electron microscope (HAADF-STEM) image given in Figure 3c shows bright spots which are referred to as heavy Fe atoms. These existences of Fe are consistent with the energy dispersive spectroscope (EDS) measurements, as shown in Figure S10 (Supporting Information). The bright spots are uniformly distributed and their size is ≈1 Å which confirms the presence of single Fe atoms. Besides, the homogeneous distribution of Fe and N species in Fe@NC is further revealed by electron energy-loss spectroscopy (EELS) mapping images, as shown in Figure 3d. The contents of Fe atoms in Fe@NC were 0.74 wt% as per coupled plasma optical emission spectrometry (Table S3, Supporting Information).

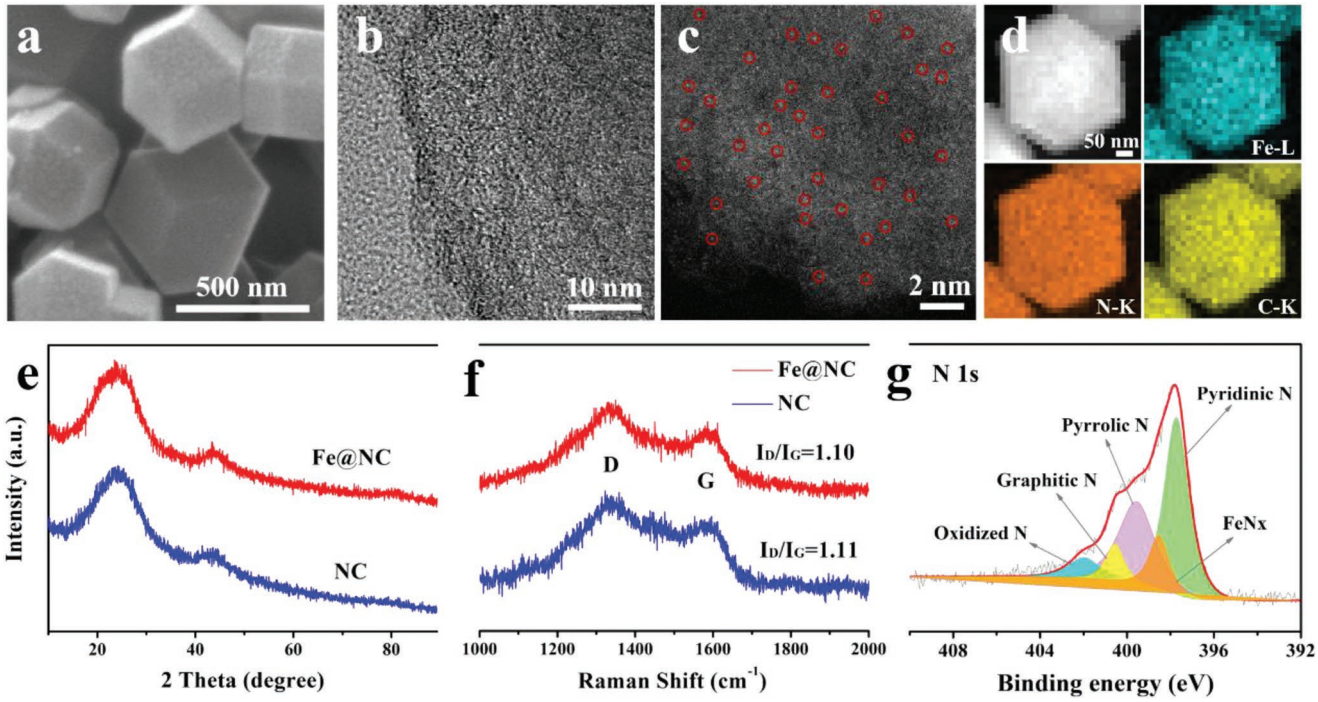

Figure 3. Compositional and structural characterization of Fe@NC. a) SEM, b) HRTEM, and c) HADDF-STEM images of Fe@NC where the single Fe atoms are highlighted in red circles. d) EELS mapping images of C, N, and Fe in Fe@NC, demonstrating the homogeneous distribution of single Fe atoms on Fe@NC. e) XRD patterns, f) Raman spectra, and g) XPS N 1s spectrums of Fe@NC and NC.

In X-ray powder diffraction (XRD) patterns of both Fe@NC and NC (Figure 3e), there are only two broader diffraction peaks centered at ≈24.5° and ≈43.3° which correspond to partially graphitized carbon. The XRD patterns did not show any peak for Fe. These results are in accordance with HRTEM outcomes and confirm that there is no change in the structure of NC after Fe doping. Raman spectra of Fe@NC and NC shown in Figure 3f gives the intensity ratio of D to G bands (I_D/I_G) which is 1.11 for Fe@NC and 1.10 for NC. This suggests that the introduction of a single Fe atom may not increase the detectable defects in NC. As results suggested in Figure 2,b, the introduction of Fe atom may not change the structure of the matrix. The chemical states of Fe@NC (Figure S5, Supporting Information) are studied using X-ray photoelectron spectroscopy (XPS). Considering the measurement depth and accuracy of XPS, the peaks of Fe can hardly be detected. The high-resolution XPS N 1s spectrum given in Figure 3g suggests the co-existence of pyridinic nitrogen (≈398.2 eV), pyrrolic nitrogen (≈400.0 eV), graphitic nitrogen (≈401.0 eV), and oxidized nitrogen species (≈402.9 eV). Notably, there is an additional peak in the Fe@NC spectrum at ≈398.5 eV which is ascribed to the coordination between Fe and N. This peak manifests the presence of FeN_x species. All these results evidence the homogeneous distribution of single Fe atoms in Fe@NC with Fe-N_x-C configurations which can potentially promote the uniform deposition of Li metal.

2.3. Electrochemical Validation of the Dendrite-Free Fe@NC

Ex situ scanning electron microscopy (SEM) analysis of prepared samples was conducted to investigate their structural and morphological characteristics after plating. Coin cells with Cu, NC, and Fe@NC as working electrodes and Li foils as counter and reference electrodes, were assembled. The rough and heterogeneous surface displays anomalous Li clumps and sheet-like dendrites (**Figure 4**a) for deposited Li as 0.1 mAh cm^{-2} with Cu electrode at a current density of 0.01 mA cm^{-2} (Figure S6, Supporting Information). This outcome implies the existence of isolated and heterogeneous nucleation sites of Li metal. On the other hand, the internal and uniform lithiophilic sites of Fe@NC and NC electrodes, and their porous features favor the Li deposition inside the microstructures of these materials.

Figure S7a (Supporting Information) provides a direct and strong evidence that Li is prone to deposit and grow in the initial nucleation sites. With continual deposition of Li, the particles keep growing and aggregating with each other to cover the surface of matrix and the gaps. However, Li tends to cluster together due to the small Li adsorption energy (Figure S7b, Supporting Information). Figure 4e exhibits that the metallic Li is clung to the surface of the Fe@NC electrode; whereas, its morphology is gossamer on the NC electrode. This further confirms that the Li adsorption energy is increased after doping of single Fe atoms. Moreover, owing to the porous framework structure of NC and Fe@NC, Li might be plated into the inner place of the electrode which will decrease the amount of deposited Li on the surface, and restrict the formation of dendrites. To collect the evidences, the capacity density of Li deposition was decreased to 0.01 mAh cm^{-2} for NC electrode and 0.02 mAh cm^{-2} for Fe@NC electrode, and the region closer to the collector was studied. A large amount of plated Li was found on the Fe@NC electrode as compared to NC electrode (Figure S8, Supporting Information).

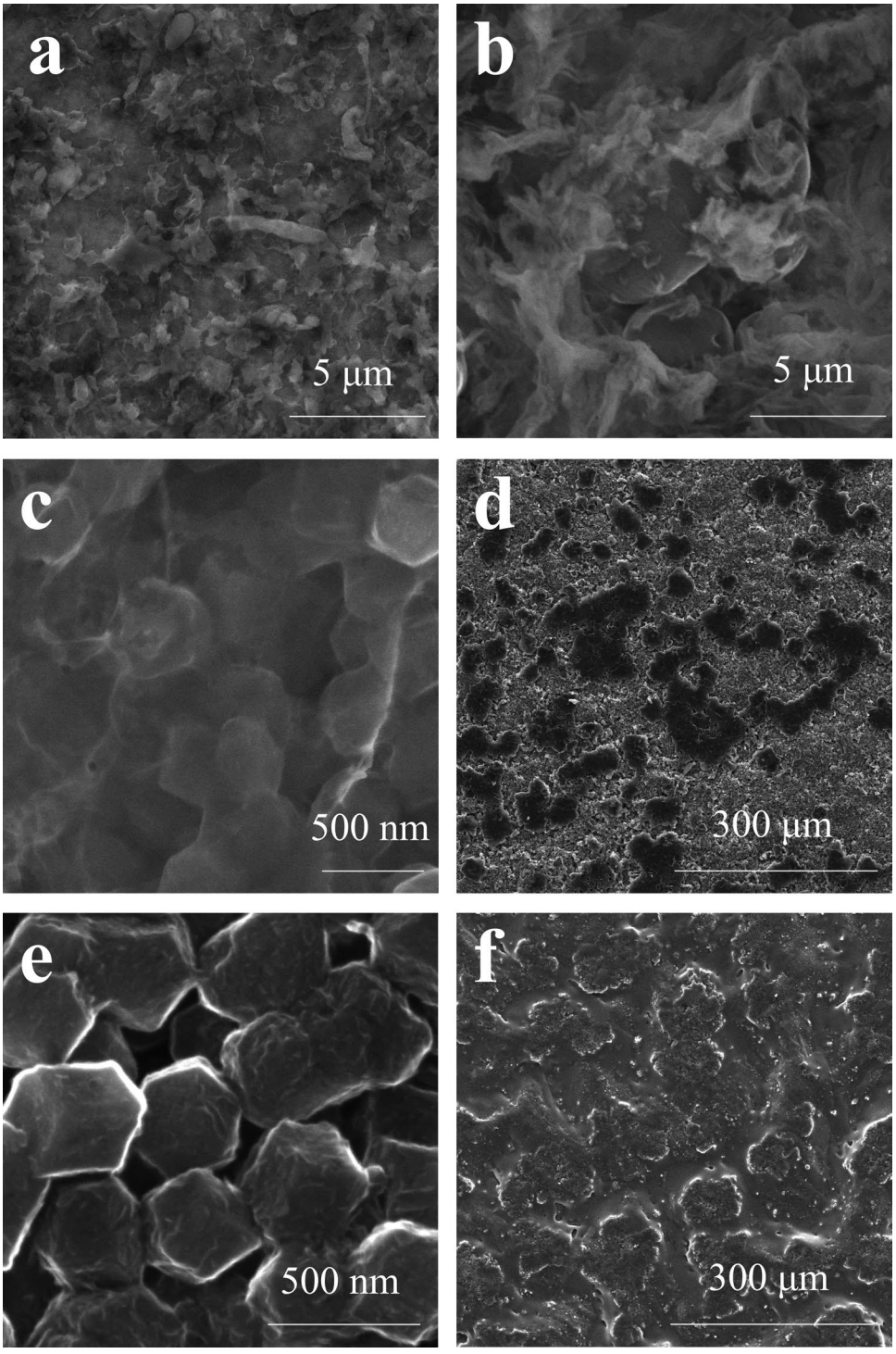

Figure 4. Nucleation and deposition characteristics of Li metal. SEM images of a) Cu, b) NC, and c) Fe@NC electrodes after 0.1 mAh cm^{-2} Li deposition at a current density of 0.01 mA cm^{-2}. SEM images of d) Cu, e) NC, and f) Fe@NC electrodes after Li deposition at a current density of 1 mA cm^{-2}.

The lithium-ion would have combined with one electron and deposited on the electrode surface at initial stage. Afterward, the deposited Li atom might have influenced the subsequent Li atoms. As given in simulation section, the diffusion barrier energy of Fe@NC is much smaller than that of NC; hence, Li atoms can easily diffuse into the inner place of the electrode. The higher Li adsorption energy of Fe@NC also contributes in attracting the Li atoms. Besides, if the current density and lithiation capacity are increased respectively up to 1 mA cm^{-2} and 1 mAh cm^{-2}, the Cu electrode gets full of Li dendrites (Figure 4b). Moreover, some isolated and spot-like Li metal islands can also be found on NC surface (Figure 4d). In

contrast, a uniform thin layer of Li is deposited on the surface of Fe@NC instead of flocking together, and it remains dendrite-free, as shown in Figure 4f. To further observe the lithium dendrite growth from cross-section, the Li-deposited electrodes were cut down the middle. Many Li dendrites can be seen on Cu electrode (Figure S11a, Supporting Information). For NC electrode, Li dendrites are full of the gap of NC materials (Figure S11b, Supporting Information). On the contrary, the Li is well restrained in Fe@NC electrode and no dendrites can be seen in the cross-section of Fe@NC (Figure S11c, Supporting Information), which is in accordance with Figure 4.

2.4. Electrochemical Performance of Fabricated Batteries

Nucleation overpotential is influenced by the lithiophilicity and nucleation rate of different hosts. It is equivalent to the difference between bottom of voltage drop and flat part of voltage plateau. Here, the Li nucleation overpotential on bare Cu, NC, and Fe@NC electrodes has been investigated (**Figure 5**a). As the current density is increased up to 2 mA cm^{-2}, the overpotential of Cu electrode at initial stage of nucleation is as high as ≈190.7 mV. Owing to the established electric field, Li ions are shifted from electrolyte to electrode surface and begin to nucleate. The nucleation sites for Li depositions are isolated and aimlessly distributed owing to the higher nucleation overpotential of electrode. After the nucleation starts, the subsequent Li ions are prone to plate on the formed nucleation sites which leads to the growth of Li dendrites. Yet, with favorable lithiophilicity, a matrix may tend to decrease the Li nucleation overpotential.

The voltage curve of NC electrode exhibits a lower nucleation overpotential of ≈37.8 mV owing to its relatively large Li

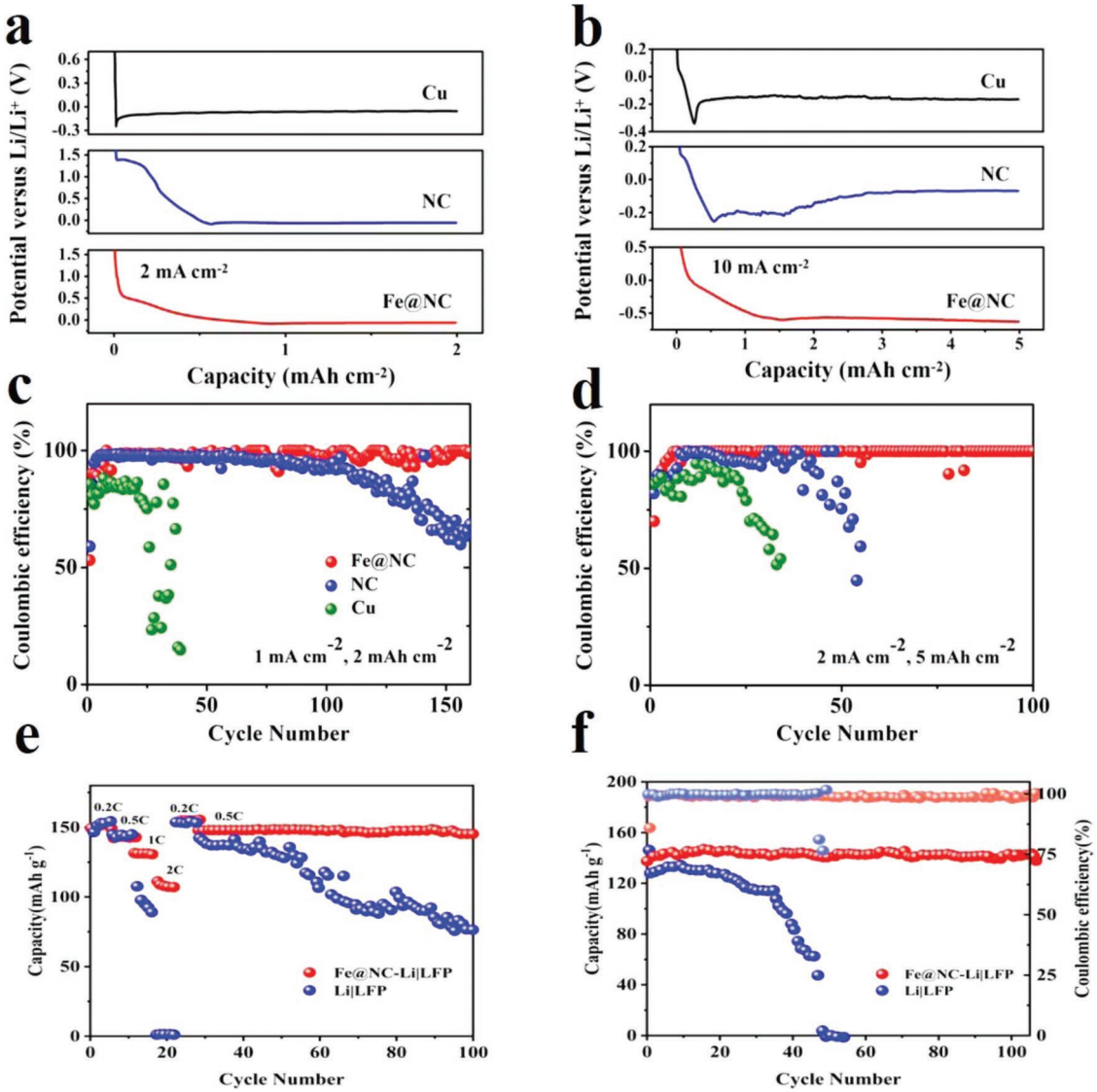

Figure 5. Electrochemical performance of Li metal battery. Nucleation overpotential of metallic Li on Cu, NC, and Fe@NC electrodes at respectively current density and capacity of a) 2 mA cm^{-2} and 2 mAh cm^{-2}, as well as b) 10 mA cm^{-2} and 5 mAh cm^{-2}. Coulombic efficiency of Fe@NC, NC, and Cu electrodes at a current density of c) 1 mA cm^{-2} with cycling area capacity of 2 mAh cm^{-2}, and d) 2 mA cm^{-2} with cycling area capacity of 5 mAh cm^{-2}. e) Rate capability performance of full cells with $LiFePO_4$ as cathode and Fe@NC/Li as the anode, and f) long-term cycling performance at 0.5 C.

adsorption energy. In contrast, the voltage curve of the Fe@NC electrode displays no obvious voltage dip. This phenomenon can further be observed when the current density reaches 10 mA cm^{-2} (Figure 5b). The nucleation overpotential of metallic Li deposition on bare Cu and NC electrodes is recorded as ≈195.3 and ≈183.8 mV, respectively. Where, the overpotential of Fe@NC electrode remains only ≈34.1 mV, implying the superior contributions of Fe interfacial sites. The high lithium plating potential for anode material will increase the cathode potential in full cell, thus improving the capacity of the cell. Meanwhile, the potential of lithium dendrite formation is 0 V (Li^+ vs Li). The potential difference between Li plating (for Fe@NC) and Li dendrite formation will be huge. Therefore, under the condition of large polarization, it is still hard to form Li dendrites.

Simulation study evidences that the single Fe atom doping increases the adsorption energy of Li for localized regions around the doping sites. Hence, it becomes appropriate for metallic Li to be plated uniformly on the electrode surface instead of growing at inner nucleation sites. Moreover, the overpotential at a varying current density from 0.1 to 10 mA cm^{-2} exhibits similar results (Figure S9, Supporting Information). The nucleation overpotential of Cu electrode remains higher at different values of current density. At low current density, both NC and Fe@NC electrodes display low overpotential values. Nevertheless, with an increase in current density, the overpotential of NC electrode increases rapidly, but that of Fe@NC electrode, remains lower, suggesting that Fe@NC may have a positive effect on fast-charging field.

The Coulombic efficiency is often considered as an index to appraise the sustainability of Li metal anodes. It is, actually, the ratio of the amount of stripped Li metal to the amount of platted Li metal. For current density of 1 mA cm^{-2} and capacity of 2 mAh cm^{-2}, it increases for Fe@NC electrode from 53.15% to 98.28% during 6 cycles and then remains stable at ≈97.4% for ≈160 cycles. The irreversible capacity loss could be the result of notable specific surface area and the formation of stable SEI on the surface of electrode. Moreover, the Coulombic efficiency of NC and Cu electrodes is extremely unsteady and decreases to 85% respectively after 120 and 20 cycles, which can be attributed to the uncontrolled growth of Li metal. This phenomenon can also be observed when the current density increases to 2 mA cm^{-2}, and capacity to 5 mAh cm^{-2} (Figure 5d). The Coulombic efficiency of the Fe@NC electrode still remains stable at ≈99.0% for 100 cycles; however, its value for Cu and NC electrodes drops drastically. These results demonstrate that single Fe atom doped Fe@NC electrodes can deliver excellent reversibility and discourage the Li dendritic growth during the charge/discharge process.

To further examine the applied function of Fe@NC anode in lithium metal batteries (LMBs), we assembled the Fe@NC/Li and Li anodes with $LiFePO_4$ (LFP) cathode. The discharge capacity of a bare Li/LFP battery at a low rate (0.2–0.5 C) is similar to that of a Fe@NC/LFP cell (Figure 5e). But when under the high current density, the Fe@NC/LFP battery offered a high discharge capacity of 132 mAh g^{-1} at 1 C (1 C = 170 mA g^{-1}) and remained at 110 mAh g^{-1} at even higher rate of 2 C, which is significantly greater than Li/LFP cells. At the rate of 0.5 C, the Coulombic efficiency of typical Li/LFP cell drops <60% after 30 cycles due to irreversible Li consumption during cycling (Figure 5f). The Fe@NC/LFP full cell shows a relatively improved performance compared to Li/LFP cell, with the initial capacity of 146 mAh g^{-1} at 0.5 C. Moreover, it delivers a retention rate of 98% (143 mAh g^{-1}) and Coulombic efficiency as high as 99.72% after 100 cycles. These results reveal that Fe@NC has a great potential to work as a worthful host for Li metal anode, and together with LFP cathode, it offers enhanced cycling stability and rate performance at higher rates; these results indicate its remarkable application in high-performance energy storage systems.

3. Conclusion

To sum up, ZIF-8 is employed as a carrier for single iron (Fe) atoms to control the nucleation and deposition features of Li metal. The Li atoms are inclined to plate into the inner space of Fe@NC electrode owing to the increased adsorption energy, reduced nucleation barrier, and enhanced diffusion capacity of Li. Besides, the specific framework structure of Fe@NC can hinder the Li growth in one direction and restrain the volume expansion of Li metal, thus, delivering a dendrite-free morphology. Consequently, the Fe@NC electrode displays an excellent reversibility and much higher capacities without degradation of other properties. Moreover, when it is coupled with $LiFePO_4$ cathode, the assembled full cell also exhibits remarkable cycling stability as well as the rate performance. The boundary dimension and pore size of Fe@NC could be the critical factors for the fabrication of an efficient battery. In this regard, further investigation is desirable to optimize the structure of matrix. The current work enlights new sights for the development of high-performance and fast-charging lithium metal batteries.

4. Experimental Section

Synthesis of Fe@NC: Methanol solutions (45 mL)of 2-methylimidazole (1314 mg, 16 mmol), $Co(NO_3)_2{\cdot}6H_2O$ (1190 mg, 4 mmol), and $Fe(acac)_3$ (141 mg, 2.4 mmol) were prepared through vigorous stirring for 1 h at room temperature. Subsequently, the former solution was moved to a 100 mL Teflon lined stainless-steel autoclave where it was heated at 120°C for 4 h. The mixture was rinsed with DMF for three and methanol for two times. After drying the faint yellow solid at 70 °C overnight, Fe-ZIF-8 was assembled in powder form. The pyrolysis of Fe-ZIF-8 was carried out in a tube furnace filled with argon gas. The temperature of the furnace was increased at a heating rate of 5 °C min^{-1}. The sample was heated at 900 °C for 3 h and then it was cooled to room temperature naturally. The NC powder was prepared using the same method except without addition of $Fe(acac)_3$.

Material Characterization: To observe the Li dendrites, the coin cells after plating were unclosed in Ar-filled glove box. Fe@NC and Cu electrodes were washed with fresh dimethyl carbonate and dried subsequently. The treated electrodes were placed on stages and packed in a glove box, after which these were transferred immediately for scanning electron microscope (SEM, HITACHIS-4800, Japan) to observe the morphology and structure of electrodes. Whereas, field emission transmission electron microscope (Tecnai G2 F20 S-Twin, USA) was employed to investigate the microstructures and elemental disseminations. X-ray photoelectron spectroscopy (XPS) was employed on a PHI instrument (PHI 5000 VersaProbe, Ulvac-Phi, Japan) which

uses monochromatic Al Kα radiation (225 W, 15 mA, 15 kV) to trace the species of nitrogen atoms and the composition of Fe@NC. Shirley-type background subtraction was employed to get the curve fitting of XPS spectra. During Raman spectroscopy analysis, Raman spectrometer (LabRam HR800-UV-NIR, HORIBA JobinYvon, Paris, France) with excitation laser wavelength 532 nm was used.

First Principles Calculations: The computational simulation module CASTEP and functionals GGA and PBE were employed in this study. Considering the calculation time and computer performance, the calculation accuracy was set to coarse. The calculated cut-off energy was set as 10 eV, and the *k*-point was set as $1 \times 1 \times 1$. The pressure tolerance, force tolerance, energy tolerance, and maximum displacement were respectively set as 0.2 GPa, 0.1 eV Å^{-1}, 5.0×10^{-5} eV per atom, and 0.005 Å, and the maximum iteration was set as 100. In addition, the SCF tolerance and maximum SCF cycle are set to 1.0×10^{-5} eV per atom and 1000, respectively. The formula for the determination of adsorption energy of lithium atoms is:

$$E_{ab} = E_{total} - E_{sub} - E_{Li} \quad (1)$$

Where, E_{total} represents the total energy of the system after adsorption of lithium, E_{sub} represents the total energy of substrate, and E_{Li} represents the energy of a single lithium atom.

Electrochemical Measurement: CR2025-type coin cells were fabricated using Cu foils, NC@Cu and FeNC@Cu as working electrodes and Li foils as counter electrode. The assembly of these cells was achieved in Ar-filled glove box with oxygen and water vapor contents <0.1 ppm. Here, 1 M LITFSI in DME/DOL (1:1 w/w) was used as an electrolyte. The electrolyte amount was ≈100 ± 10 µL. For half-cell testing, the slurry of FeNC powder and polyvinylidene fluoride (PVDF) binder (mass ratio 8:2) in N-methylpyrrolidone (NMP) was coated on a Cu foil and dried in vacuum. The loading of Fe@NC and NC was 3.5 ± 0.2 mg cm^{-2}. As-obtained sample was punched into disks having a diameter of 13 ± 0.1 mm. A layer of Celgard separater (Celgard 2400, 25 µm thick) was inserted between working electrode and counter electrode to separate them electrically. For Coulombic efficiency determination, a measured quantity of Li was loaded on anode and stripped up to 3 V for each cycle. The calculation of the overpotential can be defined as the difference between the tip and the platform.

In full cell testing, $LiFePO_4$ (LFP) was used as cathode and bare Li metal or Fe@NC composite as anode. For LFP cathode (1.0 C = 170 mA g^{-1}), a slurry with LFP powders mixed with super-P and PVDF at a weight ratio of 8:1:1 in NMP was coated on Al foil and dried in vacuum. The loading of $LiFePO_4$ was ≈3 mg cm^{-2}, while the loading of Fe@NC was ≈3.5 mg cm^{-2}. One molar $LiPF_6$ in ethylene carbonate/diethyl carbonate (1:1 v/v) was used as an electrolyte. The amount of electrolyte was ≈100 µL. The voltage test ranges of Li/LFP cells were 2.5–3.9 V.

Statistical Analysis: In the first few cycles of Figure 5c–f, the coulombic efficiency and capacity are relatively low due to the activation process of battery. The sample size for SEM image is two units, while the sample size for cycle performance is three units. Two side hypothesis test is used to evaluate whether there is overpotential difference between Fe@NC and NC or Cu matrix under the current density of 10 mA cm^{-2}. If there is no overpotential difference among the three matrices, the alpha value is 0.05. As calculated by Mini-Tab, both probability (*P*) values are <0.01, which indicates that the overpotential difference between Fe@NC and NC or Cu matrices is significant.

Supporting Information

Supporting Information is available from the Wiley Online Library or from the author.

Acknowledgements

This work was supported by National Natural Science Foundation of China (Grant Nos. 51972330), the Military Commission Logistics Department (Grant Nos. BY117J013), the State Key Program of National Natural Science Foundation of China (Grant No. 61734008), and the Natural Science Foundation of Jiangsu Province (Grant No. BK20210129). The authors are grateful to Platforms of Characterization & Test, Collaborative Innovation Center of Suzhou Nano Science and Technology, and Nanofabrication Facility from Suzhou Institute of Nano-Tech and Nano-Bionics, for their technical support and provision of experimental facilities.

Conflict of Interest

The authors declare no conflict of interest.

Data Availability Statement

The data that support the findings of this study are available from the corresponding author upon reasonable request.

Keywords

carbon framework, Li metal batteries, nucleation overpotential, single iron atom, ZIF-8

Received: June 8, 2022
Revised: August 5, 2022
Published online: September 9, 2022

[1] J. M. Tarascon, M. Armand, *Nature* **2001**, *414*, 359.
[2] J. B. Goodenough, Y. Kim, *Chem. Mat.* **2010**, *22*, 587.
[3] C. K. Chan, H. L. Peng, G. Liu, K. McIlwrath, X. F. Zhang, R. A. Huggins, Y. Cui, *Nat. Nanotechnol.* **2008**, *3*, 31.
[4] Y. S. Hu, P. Adelhelm, B. M. Smarsly, S. Hore, M. Antonietti, J. Maier, *Adv. Funct. Mater.* **2007**, *17*, 1873.
[5] C. Z. Zhao, P. Y. Chen, R. Zhang, X. Chen, B. Q. Li, X. Q. Zhang, X. B. Cheng, Q. Zhang, *Sci. Adv.* **2018**, *4*, 3446.
[6] M. H. Bai, K. Y. Xie, K. Yuan, K. Zhang, N. Li, C. Shen, Y. Q. Lai, R. Vajtai, P. Ajayan, B. Q. Wei, *Adv. Mater.* **2018**, *30*, 1801213.
[7] S. C. Wu, Y. Qiao, S. X. Yang, M. Ishida, P. He, H. S. Zhou, *Nat. Commun.* **2017**, *8*, 15607.
[8] D. S. Geng, N. Ding, T. S. A. Hor, S. W. Chien, Z. L. Liu, D. Wuu, X. L. Sun, Y. Zong, *Adv. Energy Mater.* **2016**, *6*, 1502164.
[9] Q. Lu, Y. G. Gao, Q. Zhao, J. Li, X. H. Wang, F. S. Wang, *J. Power Sources* **2013**, *242*, 677.
[10] Q. F. Dong, C. Wang, M. S. Zheng, *Prog. Chem.* **2011**, *23*, 533.
[11] P. Harks, C. B. Robledo, T. W. Verhallen, P. H. L. Notten, F. M. Mulder, *Adv. Energy Mater.* **2017**, *7*, 1601635.
[12] N. Jayaprakash, J. Shen, S. S. Moganty, A. Corona, L. A. Archer, *Angew. Chem.-Int. Edit.* **2011**, *50*, 5904.
[13] K. Takechi, T. Shiga, T. Asaoka, *Chem. Commun.* **2011**, *47*, 3463.
[14] K. Hofstetter, A. J. Samson, S. Narayanan, V. Thangadurai, *J. Power Sources* **2018**, *390*, 297.
[15] K. Liu, D. Zhuo, H. W. Lee, W. Liu, D. C. Lin, Y. Y. Lu, Y. Cui, *Adv. Mater.* **2017**, *29*, 1603987.
[16] M. H. Ye, Y. K. Xiao, Z. H. Cheng, L. F. Cui, L. Jiang, L. T. Qu, *Nano Energy* **2018**, *49*, 403.
[17] X. Wang, W. Zeng, L. Hong, W. W. Xu, H. K. Yang, F. Wang, H. G. Duan, M. Tang, H. Q. Jiang, *Nat. Energy* **2018**, *3*, 227.
[18] S. S. Chi, Y. C. Liu, W. L. Song, L. Z. Fan, Q. Zhang, *Adv. Funct. Mater.* **2017**, *27*, 1700348.

[19] X. B. Cheng, T. Z. Hou, R. Zhang, H. J. Peng, C. Z. Zhao, J. Q. Huang, Q. Zhang, *Adv. Mater.* **2016**, *28*, 2888.
[20] P. C. Shi, L. C. Zhang, H. F. Xiang, X. Liang, Y. Sun, W. Xu, *ACS Appl. Mater. Interfaces* **2018**, *10*, 22201.
[21] L. Xiao, X. L. Chen, R. G. Cao, J. F. Qian, H. F. Xiang, J. M. Zheng, J. G. Zhang, W. Xu, *J. Power Sources* **2015**, *293*, 1062.
[22] K. R. Deng, D. M. Han, S. Ren, S. J. Wang, M. Xiao, Y. Z. Meng, *J. Mater. Chem. A* **2019**, *7*, 13113.
[23] N. Wu, Y. R. Shi, T. Jia, X. N. Du, Y. X. Yin, S. Xin, Y. G. Guo, *ACS Appl. Mater. Interfaces* **2019**, *11*, 43200.
[24] M. Ahmed, A. Z. Yazdi, A. Mitha, P. Chen, *ACS Appl. Mater. Interfaces* **2018**, *10*, 30348.
[25] Y. Z. Su, S. Li, D. Q. Wu, F. Zhang, H. W. Liang, P. F. Gao, C. Cheng, X. L. Feng, *ACS Nano* **2012**, *6*, 8349.
[26] F. X. Wu, J. T. Lee, Y. R. Xiao, G. Yushin, *Nano Energy* **2016**, *27*, 238.
[27] Y. Nan, S. M. Li, Y. Z. Shi, S. B. Yang, B. Li, *Small* **2019**, *15*, 1903520.
[28] H. K. Kang, S. G. Woo, J. H. Kim, S. R. Lee, Y. J. Kim, *Electrochim. Acta* **2015**, *176*, 172.
[29] C. Z. Sun, T. Wu, J. N. Wang, W. W. Li, J. Jin, J. H. Yang, Z. Y. Wen, *J. Mater. Chem. A* **2018**, *6*, 19159.
[30] K. Persson, V. A. Sethuraman, L. J. Hardwick, Y. Hinuma, Y. S. Meng, A. van der Ven, V. Srinivasan, R. Kostecki, G. Ceder, *J. Phys. Chem. Lett.* **2010**, *1*, 1176.
[31] J. Yamaki, S. Tobishima, K. Hayashi, K. Saito, Y. Nemoto, M. Arakawa, *J. Power Sources* **1998**, *74*, 219.
[32] M. M. Zhen, J. Wang, X. Wang, C. Wang, *Chem.-Eur. J.* **2018**, *24*, 5860.
[33] Y. X. Yu, *Phys. Chem. Chem. Phys.* **2013**, *15*, 16819.
[34] J. X. de Carvalho, M. S. Hussein, W. B. Li, *Phys. Rev. A* **2008**, *78*, 032906.
[35] A. V. Carpentier, Y. H. Fung, P. Sompet, A. J. Hilliard, T. G. Walker, M. F. Andersen, *Laser Phys. Lett.* **2013**, *10*, 125501.
[36] Y. B. Hao, Z. S. Shao, C. Cheng, X. Y. Xie, J. Zhang, W. J. Song, H. S. Wang, *ACS Appl. Mater. Interfaces* **2019**, *11*, 31755.
[37] H. F. Zhang, M. Zhao, Y. Yang, Y. S. Lin, *Microporous Mesoporous Mat.* **2019**, *288*, 109568.